Strengthening of a curved composite beam by introducing a flat portion

Sylvain Arki, Jean-François Ferrero, Steven Marguet, Jean-Max Redonnet, Alexandre Aury

Version of Record: https://www.sciencedirect.com/science/article/pii/S0263822318343113
Manuscript_5acf78e0af80fe0145be99ab3fe67fa9

Strengthening of a curved composite beam by introducing a flat portion

Sylvain Arki[a,1,*], Jean-François Ferrero[a], Steven Marguet[a], Jean-Max Redonnet[a], Alexandre Aury[b]

[a] *Université de Toulouse, Institut Clément Ader, UMR CNRS 5312, UPS/INSA/ISAE/Mines Albi, 3 rue Caroline Aigle, 31400 Toulouse, France*
[b] *SKF Aerospace France, 22 rue Brillat Savarin, 26300 Chateauneuf-sur-Isère, France*

Abstract

This paper deals with the effect of the introduction of a central flat zone on the mechanical strength of quasi-isotropic curved composite beams. Composite fittings, a particular kind of curved composite beams, are often used in the aeronautical industry as junction parts. In most cases, and in order to connect parallel or orthogonal panels, they present a C-, T- or L-shaped geometry. Subjected to complex loadings, including bending, they have to face out-of-plane tension in their curved region. This phenomenon, known as unfolding, can lead to unstable delaminations and to a global failure of the assembly.

In this study, a central flat zone is introduced in the curved region of a L-shaped laminated composite curved beam. Experimental results demonstrate the strengthening effect of this architecture, with a rise in the mechanical strength of around 15%. A finite element model, based on continuum mechanics and cohesive zones model, is developed. After dealing with the difficulties met with cohesive zones model and mesh size dependency, the proposed model presents results in agreement with experimental observations. It enables the understanding of the differences between the failure scenarii of the original and modified curved composite specimens.

Keywords: curved laminated composite, unfolding, delamination, cohesive zones model, finite element method

1. Introduction

Composite materials represent a significant and growing portion of the materials used in the aerospace industry. Nowadays, the percentage of mass of composites in the last generation of aircraft structures, such as Boeing 787 and Airbus A350, reaches almost 50% of the overall mass. This increasing use is due to the high specific stiffness and strength and to the advantageous fatigue behaviour in comparison with metals.

Connecting parts, such as fittings, are concerned with that transition to composite materials. These parts are of various shapes, like, C-, L- and T-shaped for instance, as illustrated in Fig. 1a. They are used to connect distant parallel panels (C-shaped fittings) or perpendicular panels (L- and T-shaped fittings). They can be subjected to severe and at spatially complex loadings that lead to overall bending. An important consequence is the appearance of out-of-plane normal tension and shear stresses that tend to delaminate the curved regions of the parts as presented in Fig. 1b.

The design and sizing of optimized shapes to prevent this phenomenon of delamination induced by unfolding imply to be able to accurately predict the behaviour of these structures until failure. This point is essential to ensure the fittings will not fail in flight.

One of the most commonly studied geometry of curved composite beam over the fifty last years is presumably the L-shape. In the last fifty, Lekhnitskii [1] proposed a calculation method based on beams theory in order to determine the transverse tension state and the Curved Beam Strength (CBS: the moment per unit width which causes a sharp decrease in the applied load) of a L-shaped beam made of 0° unidirectional composite plies, loaded with four-point bending. This method is now part of the ASTM D6415/6415M standard [2] which proposes a procedure to experimentally determine the CBS. Kedward et al. [3] compared Lekhnitskii [1] analytical approach with a simplified one and with a 2D finite element analysis. They obtained similar results with low dispersion between the three calculation methods. Later, Shenoi and Wang [4] proposed an extended calculation method in order to determine the repartition of the radial and tangential stresses in curved composite beams made of 0° and 90° unidirectionnal plies. They have highlighted the significant effect of the arc and of the stacking sequence on the through-thickness stresses distribution and on delamination for

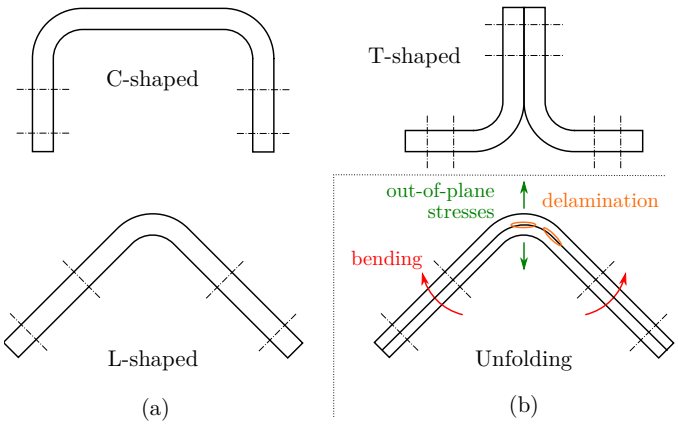

Figure 1: (a) Usual fitting geometries (b) Delamination by unfolding

*Corresponding author
Email address: sylvain.arki@univ-tlse3.fr (Sylvain Arki)

relatively thin (up to 4 plies) laminates. Kress et al. [5] and Roos et al. [6] developed an analytical model to compute the interlaminar normal stress, by taking into account the interlaminar shear stress, in singly curved composite beams loaded in tension (unfolding) or compression (folding). They validated their model with reference finite element solutions and compared the results obtained with experiments made on unidirectional and cross-ply laminated specimens. They shown that, in tension the failure was located at the centre of the arc (predominance of out-of-plane interlaminar normal stress) whereas in compression it was in the arms, at the junction with the arc (predominance of out-of-plane interlaminar shear stress). They also pointed out the difficulties met with cross-ply laminated specimen, where intralaminar transverse matrix cracking was observed prior to delamination, contrary to what was expected. More recently, González-Cantero et al. [7] obtained similar results compared to Lekhnitskii [1] with a new approach based on the compatibility and equilibrium status at the interfaces of the plies. They also confirmed the discontinuity of the shear stresses on some interfaces calculated by Shenoi and Wang [4].

Based on Lekhnitskii [1], Kedward et al. [3] demonstrations and ASTM procedure, several authors such as Cui et al. [8], Hao et al. [9], and Charrier et al. [10] identified the CBS experimentally with four-point bending tests on several kind of specimens and laminates. Cui et al. [8] have tested E-glass armed semicircular specimen. They observed sudden failures by delamination with an onset located in the centre of the arc near the middle of the thickness. Despite the dispersion of experimental results, they were able to show that the method proposed by Kedward et al. [3] was providing relevant approximations of the interlaminar tensile strength (ILTS) for 0° laminates.

Hao et al. [9] studied L-shaped specimens made of 20, 40 and 60 plies of carbon-epoxy prepreg with a [45/0/0/-45] layup pattern, intermediate 90° separation plies, laminate symmetry and with various radius over thickness ratios. They shown that the CBS increased significantly with the thickness and slightely with the radius over thickness ratio. It was the opposite for the maximum radial stress due to the presence of more flaws and larger residual stresses in the thickest specimens. Moreover, they observed brittle failures by delamination located in the 0/0° interfaces for all the configurations. For the thinest specimens, delamination started at several interfaces at the same time whereas for thicker specimens delamination was starting nearby the middle of the arc at mid-thickness and then occuring in upper and lower interfaces. According to Borg et al. [11], this phenomenon can be explained by the fact that the interface toughness of a 0/0 interface is four times lower than the one of a 0/90 and two times lower than the one of a 45/-45.

More recently, Charrier et al. [10] studied L-shaped specimens of various thicknesses (16, 32 and 48 plies of 0.262 mm thickness) but with constant radius over thickness ratio. They used highly oriented ($[(0_3/45/90_2/135/0)_n]_s$, highly disoriented ($[(45_2/0/135_3/90/45)_n]_s$), quasi-isotropic ($[(45/90/135/0)_{2n}]_s$) and unidirectional ($[0_{8n}]_s$) carbon/epoxy laminates (where the subscript n stands for the number of repetitions of the stacking sequence pattern and the subscript s stands for symmetric). To identify the CBS, they have extracted the maximum out-of-plane tensile stress computed by a three dimensional linear elastic finite element model at the experimental failure load. They concluded that the stacking sequence of the laminate had no significant incidence on the observed strength, so as the thickness of the laminate once it was thick enough to avoid bending of the arms in four-point bending. For the 48 plies specimen a lower material strength was found, attributed to non suitable curing cycle for such thick specimens. The same analysis was provided by Hao et al. [9]. The delamination was found to initiate between the 1/4 and the 1/2 of the thickness (starting from the inner arc) as a function of the stacking sequence but at constant relative position for a given layup on different thickness. Once again, the observed failures were sudden, with a pronounced load drop. Another configuration was studied by Kim et al. [12] on C-shaped beam of height 200 and 400 mm made of unidirectional carbon-epoxy prepreg USN150B and quasi-iso layups ($[(45/90/\text{-}45/0)_n]_s$, 24 and 48 plies). The specimens were loaded in tension in order to open the C. As a result, the curved zones were not subjected to pure bending as it is the case in four-point bending tests. With the help of a geometrically non-linear three dimensional finite element model, and in agreement with experimental observations, the authors highlighted a failure due to delamination located at an angle $\theta \simeq 70°$ corresponding to a maximum out-of-plane normal and shear stresses mix (θ varying from 0 to 90° in the curved region). They explained this phenomenon by the fact that if the maximum out-of-plane normal stress is located in the middle of the arc at approximately one third of the thickness starting from the inner arc, the maximum out-of-plane shear stress is encountered at the junction between the curved and the plane areas.

At last, the modelling of delamination on curved composite beams remains a challenging problem. Gözlüklü and Coker [13] used Cohesive Zone Method (CZM) with bi-linear cohesive zones damage model for mode I, mode II and mixed mode delamination [14] on L-shaped laminate made of 24 unidirectional carbon-epoxy plies oriented at 0°. The dynamic propagation of a crack located at the mid-height of the specimen was investigated with two dimensional implicit and explicit finite element models built under plane strain assumption. Even if the domain was quite small (L-shaped specimen 3 mm thick, with internal radius of 5 mm and arms of 10 mm length), and even if cohesive elements were used only in the interface located at mid-height with an initial crack of 1 mm in the centre of the arc, the fine mesh discretization (mesh size of 0.125 mm) lead to long computation times of around 10 hours. Since the specimen was blocked at the extremity of one arm and loaded parallel to the other arm, the crack propagation was not symmetric. On the embedded arm, the crack propagated under complex mixed mode with a predominance of shear whereas on the loaded arm, the crack propagated under normal stress opening loading. The authors also shown that the crack tip speed was higher under shear dominating mode.

Nguyen et al. [15] proposed an extension of this approach to simulate the unfolding, under four-point bending tests, of L-shaped carbon-epoxy laminated specimens with a stacking sequence $[(45/0/\text{-}45/90)_3]_s$ for an average thickness of 3.288 mm. They built a non-linear three dimensional finite element model,

where the plies were elastic orthotropic media (no intralaminar degradation) and where all the interfaces were modelled with cohesive elements under the framework of cohesive zones model with bi-linear damage law. After recalling the great disparity of values used in literature to feed the cohesive zones models [14, 16–18], they investigated the influence of various interfacial stiffness and strengths on the response of their structure. Due to the fine mesh used, they reduced the width of the specimen to 5 mm, leading to computation times up to seven days on modern and high-performance computer. Among all the combinations of parameters investigated, a few made it possible to reproduce the failure observed experimentally with a satisfactory level of precision, that is to say multiple cracks with delamination close to the inner arc and most of the time located at interface between 90 and ±45° plies, between the centre of the arc and the transition zone with the arm (mixed mode failure). As an interesting point, it was shown by the authors that the best set of parameters used to reproduce DCB tests was not necessarily the most suitable for the simulation of four-point bending.

As can be seen from this review, most research works have focused on understanding and characterizing the ruin of curved composite beams. In this study, a simple improvement for the curved zone of a composite beam is proposed. A flat region is introduced at the center of the arc. The configuration of the part then changes from: arm, arc of 90°, arm (L-shaped) to: arm, arc of 45°, flat area, arc of 45°, arm (Fig. 2). This specimen is called M-shaped specimen in the following.

The first part is dedicated to the presentation of the specimens and of the four-point bending experimental test study carried out in order to compare the mechanical strengths of M-shaped specimens with that of standard L-shaped. The obtained results are then presented and analysed in details. In the third part, a numerical model based on three dimensional finite elements method and cohesive zones model is built in order to study the failure of both types of specimen. It provides a better understanding of what distinguishes the M-shaped specimens from the L-shaped ones in terms of failure mechanisms.

2. Specimens and test method

2.1. Specimens

The L- and M-shaped curved beam specimens are presented in Fig. 2. The L-shaped specimen is composed of two arms of length L=90 mm, linked by a curved region of radius R=5 mm and angle ϕ=90°. The M-shaped specimen is almost the same except in the middle, where the curved zone is split in two parts of angle 45° linked by a flat area of length M=10 mm.

All the specimens were made from Hexcel AS4/8552 unidirectional prepreg and laminated by hand on a moulding tool. Pressure was applied every two plies with a vaccum bag in order to avoid porosities. The specimens were cured in autoclave following the manufacturer recommendations and their final width was W=60 mm. This value was chosen in order to limit the edge effects on the measured failure load as specified by Charrier et al. [10]. At last, a side face of each specimen was painted in white to facilitate the detection of delaminations.

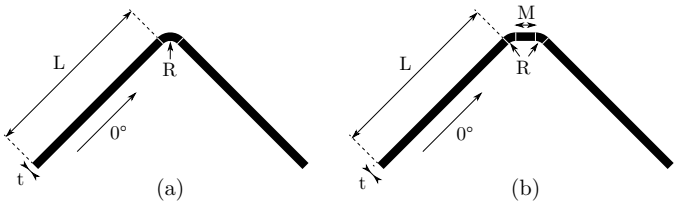

Figure 2: (a) L-shaped specimen geometry (b) M-shaped specimen geometry

A quasi-isotropic laminate sequence made of 24 plies was used. The stacking sequence was $[(45/0/\text{-}45/90)_3]_s$ where the direction 0° corresponds to the direction along the length of the arms of the specimen (Fig. 2). Since each ply was 0.18 mm thick, the global thickness of the laminate was t=4.32 mm after curing.

2.2. Test apparatus and protocol

The four-point bending apparatus presented in Fig. 3 was used to unfold the specimens. Following the principles exposed in ASTM D6415/6415M [2] recommendations, it was made of two parallel upper cylinders separated by a distance d_{top} and two parallel lower cylinders separated by a distance d_{bottom}. The diameter of the cylinders was 15 mm. To limit the sliding between the arms of the specimens and the test device, all the cylinders where placed in the apparatus with ball bearings. For L-shaped specimens d_{top} was taken equal to 75 mm and d_{bottom} to 100 mm as in the standard. For M-shaped specimens two configurations were used considering the preconisations of Charrier et al. [10]. In the first one, referenced C75/100: d_{top} and d_{bottom} were the same as for the L-shaped specimens. This was done to enable a comparison between L- and M-shaped specimen responses with the same structural loading. In the second one, referenced C85/110, the idea was to keep the same distance d between the top cylinders and the start of the curved region as for L-shaped specimens. This led to d_{top}=75+M=85 mm and d_{bottom}=100+M=110 mm.

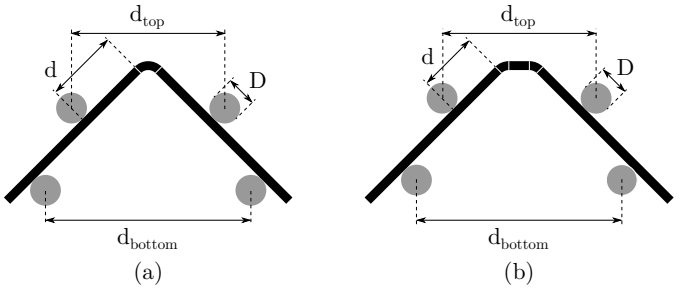

Figure 3: Test apparatus in - (a) L-shaped specimen
(b) M-shaped specimen - loading conditions

The tests were performed with an Instron 8561 hydraulic testing machine. The load signal was recorded from a ±10 kN Instron loading cell at a rate of 50 Hz and the displacement was monitored at the same rate with the LVDT sensor of the machine. In order to catch the failure scenario, a high speed

camera Photron FASTCAM SA5 was used with a speed of 150 000 images per second. An illustration of the experimental setup is given in Fig. 4.

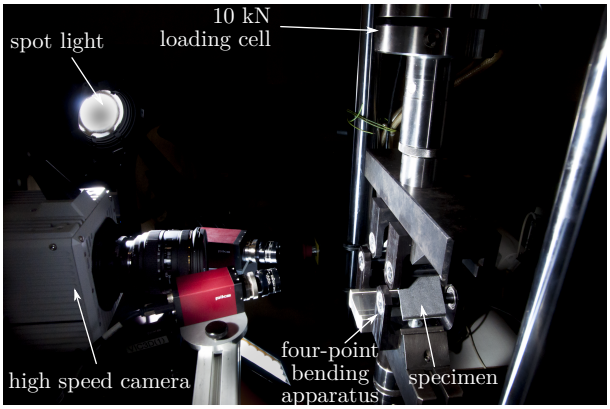

Figure 4: Experimental setup

All the specimens were loaded with a loading rate of 0.5 mm.min^{-1} and the tests were stopped at the first load drop. Each configuration was tested with at least three specimens in order to control the repeatability of the obtained results. For clarity, only the envelope curves are presented in the following figures. The lower curves, corresponding to the less loaded specimens, are post-fixed with '-L' and the upper one, corresponding to the most loaded specimen, with '-U'. At last, to measure degradation, some specimens were submitted to one cycle of unloading/reloading at various percentage of the failure load measured from previous tests. These specimens are post-fixed by 'UL' in the summary of the specimens and test conditions available in Tab. 1 (FSL: Failure Specific Load). The LR5W60UL-50% and LR5W60UL-85% specimens were respectively cycled from around 50 and 85% of the failure load.

$[(45/0/\text{-}45/90)_3]_s$ carbon-epoxy specimens				
Reference	Type	Width W (mm)	$\frac{d_{top}}{d_{bottom}}$ (mm)	FSL (N.mm^{-1}) avg / min / max
LR5W60	L	60	75 / 100	86 / 83 / 88
LR5W60UL	L	60	75 / 100	88.5 / 86 / 91
M10R5W60 C75/100	M	60	75 / 100	101.5 / 100 / 103
M10R5W60 C85/110	M	60	85 / 110	92.5 / 92 / 93

Table 1: Summary of tested configurations

3. Results and analysis

3.1. L-shaped specimens

The force per unit width ('specific' load: F/W) versus imposed displacement (u) obtained for L-shaped specimens are plotted in Fig. 5.

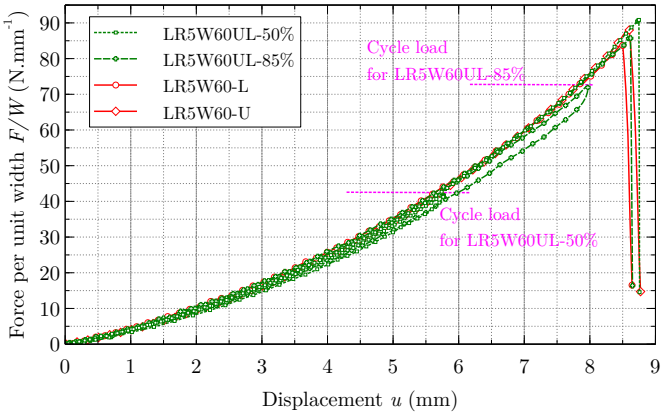

Figure 5: Load per unit width F/W versus displacement u curves for LR5W60UL and LR5W60 configurations

The first observation concerns the satisfactory level of repeatability achieved on these tests for each family of configuration with less than 6% of dispersion in terms of failure specific load and stiffness.

The curves exhibit a mechanical response in two steps. The first part is non-linear with a pronounced stiffening aspect due to geometric effects. Moreover, it can be said that it is elastic. Indeed, the LR5W60LU-50% and LR5W60LU-85% specimens did not present irreversible phenomenon before failure. The parts of the 'specific load' curves corresponding to the first loading and to the reloading look very close the one with each other. Moreover, no crack that characterizes degradation was heard during the test before failure.

The second part corresponds to the peak of load and to its brutal fall. It corresponds to a sudden delamination of some interfaces of the specimens. An illustration of what can be observed with the high speed camera is given in Fig. 6 for a LR5W60 specimen, representative of all the failures observed.

The first crack initiates in the first 90/45 interface starting from the inner arc, in the curved region near the junction with the arm, this region being loaded with a mix of out-of-plane normal and shear stresses. This corresponds to Fig. 6a which is the first image obtained with a clear delamination. These results are in good agreement with the observations made by Kim et al. [12] in the curved region of C-shaped specimen or even by Nguyen et al. [15] on L-shaped specimen. In all these studies, similar quasi-isotropic stacking sequences ($[(45/90/\text{-}45/0)_3]_s$ or $[(45/0/\text{-}45/90)_3]_s$) and specimen thickness were used with various unidirectional carbon-epoxy plies. By comparison, it seems interesting to notice that the failure scenario clearly differs from the one obtained with highly oriented laminates (almost 0° plies) such the one studied by Cui et al. [8], Hao et al. [9] and Charrier et al. [10]. In these latter cases, all the delaminations initiated in the centre of the arc, at approximately one third of the overall thickness of the specimen.

The first crack then quickly propagates of at least around 5 mm in each directions: arm and arc. This can be observed in Fig.6 b that presents the next recorded image, 6.6 μs af-

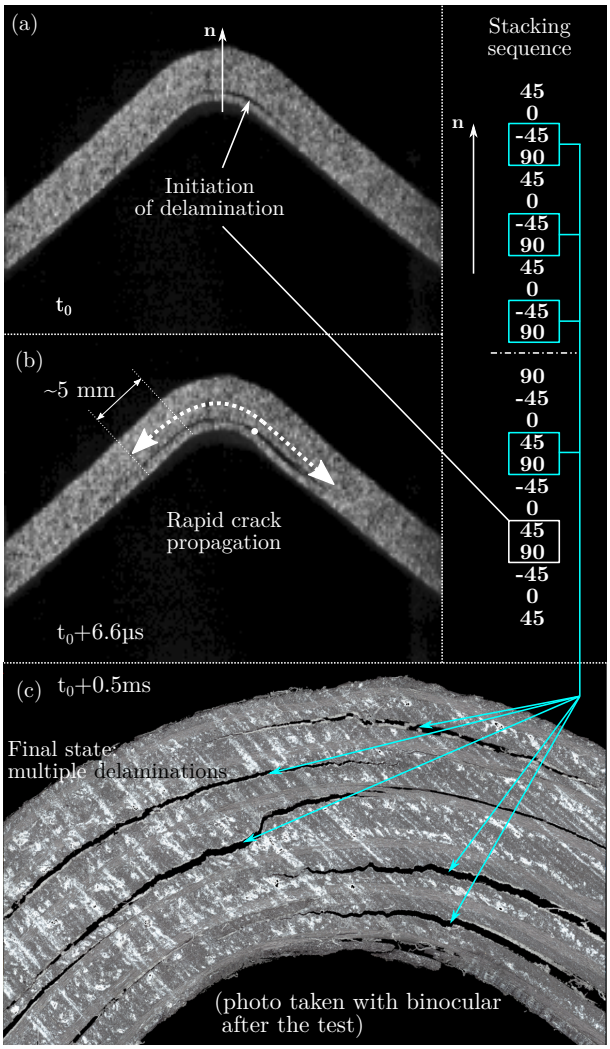

Figure 6: Typical failure scenario of L-shaped specimens. (a) Initiation (b) Propagation of the first crack (c) Final state

ter Fig. 6a. The very high speed of propagation, at least $c \simeq 5.10^{-3}/6.6.10^{-6} \simeq 750\,\mathrm{m.s^{-1}}$, is of the order of magnitude of what was measured by Gözlüklü et al. [19]: around $1000\,\mathrm{m.s^{-1}}$. This quantifies the very brittle aspect of the failure observed.

Finally, the damage state reached after less than 0.5 ms after the first obervable delamination, is shown in Fig. 6c. The specimen presents numerous 90/45 or -45/90 delaminated interfaces. Again it makes sense to compare these results, obtained on quasi-isotropic laminates, with those obtained for strongly oriented ones. In the first case, the authors Kim et al. [12] and Nguyen et al. [15] mention many broken interfaces while in the second, delamination is most often restricted to one or two interfaces [8–10].

3.2. M-Shaped specimens

In the same manner as was presented for L-shaped specimens, the specific load versus displacement curves are plotted in Fig. 7. In order to be able to make comparison between the mechanical behaviour of L-shaped and M-shaped specimens subjected to the same loading conditions (M-shaped specimens in configuration C75/100), LR5W60 specimens curves are plotted in the same graph.

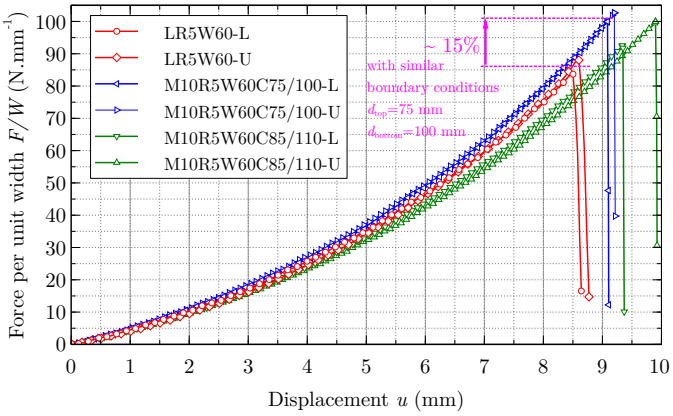

Figure 7: Load per unit width F/W versus displacement u curves for LR5W60, M10R5W60C75/100 and M10R5W60C85/110 configurations

As a first observation, the mechanical response appears to be similar for L- and M-shaped specimens. A stiffening non-linear specific load curve, followed by a sudden drop of the load due to explosive delamination, is observed. In configuration C75/100, when the cylinders present the same inter-axis for L- and M-shaped coupons, the stiffness of both kind of specimens is almost the same. Moreover, a raise of the failure load of around 15% in average (13% in the worst case) can be measured. In configuration C85/110 the stiffness is lower. This trend makes sense since the arms, more flexible, are more loaded than in C75/100 configuration. In terms of breaking load, it can be noticed that moving the upper cylinders away from the curved region also increases the failure load but with a lower extent, with an average gain of around 7%. In this latter case, it worth recalling that the loading conditions are not similar.

The second main observation arises from the analysis of the failure of the coupons. For that purpose, some photos are gathered in Fig. 8.

All the tested M-shaped specimen followed a similar failure scenario as the one observed in Fig. 6 for L-shaped curved composite beams. From Fig. 8a it can be seen an initiation of delamination in the first or the second -45/90 interface starting from the inner arc. Then, Fig. 8b highlights the rapid propagation of the delamination with a crack enlargement of approximately 5 mm in 6.6 μs. As presented in Figs. 8c and 8d, the final states of both M-shaped specimens loaded in configuration C75/100 and C85/110 present multiple -45/90 or 90/45 delaminated interfaces. However, and contrary to what was observed in Fig. 6c for L-shaped specimen, it can be noticed that the interfaces located above the two third of the height of the majority of the specimens were relatively spared. Indeed, only the -45/90 interfaces located above the mid-plane of M-shaped specimens were delaminated.

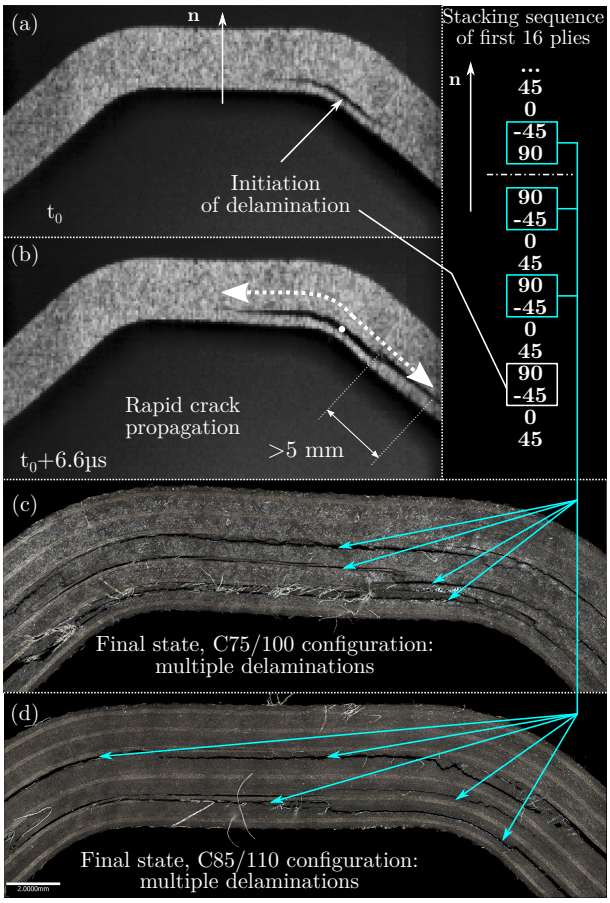

Figure 8: Typical failure scenario of M-shaped specimens. (a) Initiation for M10R5W60C75/100 (b) Propagation of the first crack for M10R5W60C75/100 (c) Final states of M10R5W60C75/100 and (d) M10R5W60C85/110

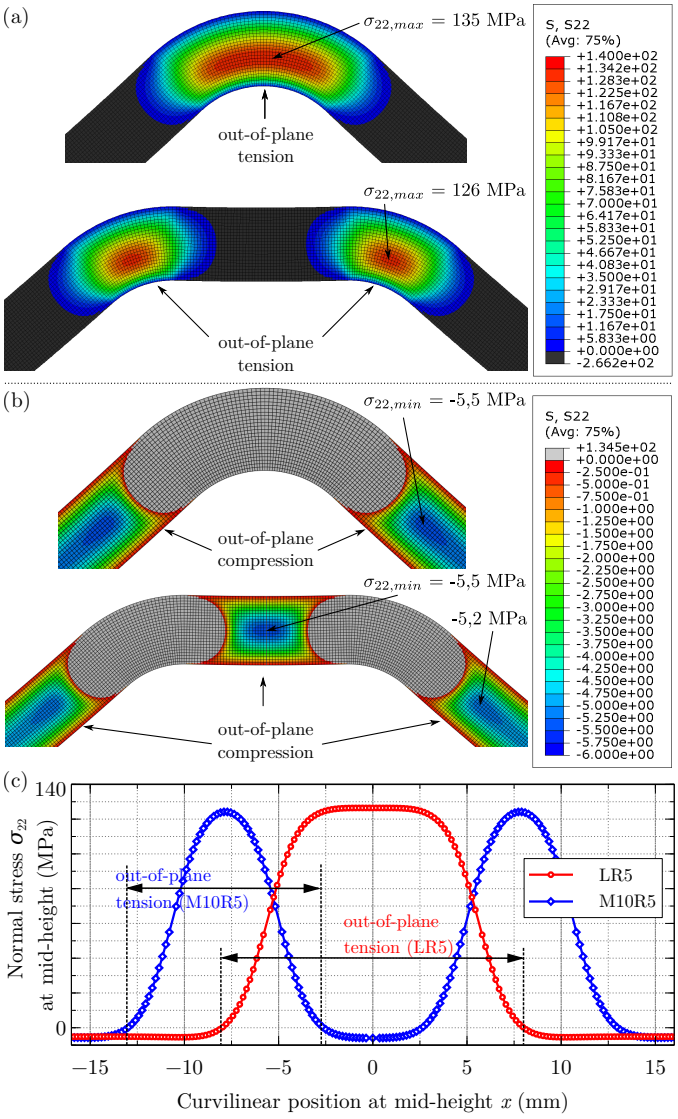

Figure 9: Transverse normal stresses in L- and M-shaped specimens
(a) Areas in tension (b) Areas in compression (c) Normal stress distribution along the curvilinear position at mid-height

In order to explain the raise in failure load obtained from L-shaped to M-shaped fitting, a simple bi-dimensional finite element model, build under the plane strain assumption, was developed. The specimen is idealized as an isotropic homogeneous aluminium like medium of elastic modulus E=70 GPa and Poisson's ratio ν=0.33. The geometry is meshed with 8 nodes quadratic, fully integrated plane strain elements of fictive thickness t=60 mm. The cylinders are analytic rigid bodies in normal contact with the arms of the specimen (no friction). The solution is computed in a geometrically non-linear framework.

The Fig. 9 presents the out-of-plane normal stresses (σ_{22}) obtained for L-shaped and M-shaped specimens under the same four-point bending loading (restricted to the curved regions). By adjusting the scales, Fig. 9a highlights the areas in out-of-plane tension whereas Fig. 9b highlights the areas in out-of-plane compression. The evolution of σ_{22} at mid-height, along the curvilinear position measured from the centre of the beam, is plotted in Fig. 9c.

The L-shaped specimen is loaded in out-of-plane compression, tension and compression. The area fully loaded in tension presents a plateau shape corresponding to an angular sector of about 90° at the mid-height of the part. The M-shaped specimen is subjected to out-of-plane compression, tension, compression, tension and compression. The two arcs loaded in tension exhibit peaks of the same intensity but reduced area, with two angular sectors of around 45°.

These observations have to be interpreted at two levels to understand the benefit coming from the introduction of the flat portion at the centre of the arc. At the material level, since the amount of transverse normal stress is the same for L- and M-shaped beams, the onset of delamination is reached and crack may occur. But at the structural level, due to the stress distribution, the opening force is twice as high in the L arc as in the M arcs. Therefore, even if the interface is damaged, the change in local load induced by the change of geometry prevents the brutal propagation of the crack.

Hence, the introduction of a flat zone in the arc enables the apparition of an area subjected to out-of-plane compression which stabilizes the curved region by reducing the opening

force that can lead to global delamination.

4. Numerical modelling of the unfolding

4.1. Modelling strategy

This section presents the three-dimensional finite element model developed to simulate the unfolding of L- and M-shaped specimens. The preprocessing, processing and analysis were performed through the use of scripts written in Python and of Abaqus/Standard finite element program.

Each ply was represented as a homogeneous orthotropic medium with one layer of three-dimensional, 8 nodes and fully integrated linear finite elements (C3D8). The width of the specimens was taken equal to W=30 mm, in order to limit the computational cost and in agreement with what is often practiced in literature [12, 15]. The thickness of the elements was set to 0.18 mm. In order to take into account the material orientation, a specific coordinate system aligned with the fibres was affected to each element of the plies. For that purpose, rectangular and cylindrical coordinate systems were used in plane and curved regions respectively.

Interfaces were introduced in the model by the use of 8 nodes hexahedra cohesive elements (COH3D8) that were extruded from the lower layer ply elements to the higher layer ply elements. The geometric thickness of these elements was null whereas the fictive associated thickness, used to compute the stiffness, was taken equal to one tenth of the thickness of the ply, that is t=0.018 mm. Each interface element had the same coordinate system as the one of its lower associated ply element.

The plies have a linear orthotropic elastic behaviour whose properties are summarized in Tab. 2.

Property	Symbol	Unit	Value
longitudinal modulus	E_l	GPa	130
transverse modulus	$E_l = E_n$	GPa	9.4
shear modulus	$G_{lt} = G_{ln}$	GPa	4.65
shear modulus	G_{tn}	GPa	4
Poisson's ratio	$\nu_{lt} = \nu_{ln}$	-	0.3
Poisson's ratio	ν_{tn}	-	0.175

Table 2: Material properties for the mechanical behaviour of the AS4/8552 ply introduced in the model

E_l, E_t, G_{lt} and ν_{lt} were identified from tests following ASTM D3039 [20] and D3518 [21] recommendations. G_{tn} was obtained from inverse identification from 3 points bending tests made on $[(45/0/\text{-}45/90)_3]_s$ specimens and ν_{ln} was taken equal to ν_{lt}. ν_{tn} was set to match transversally isotropic relationship.

The interfaces were modelled in a cohesive zones manner as classically done in literature ([14, 22, 23] for instance). The out-of-plane normal stresses σ_n and shear stresses τ_{ln} and τ_{tn} are computed from the displacement jumps between the lower and the upper nodes (δ_n, δ_l and δ_t) of the elements with a two bi-linear law as presented in Fig. 10.

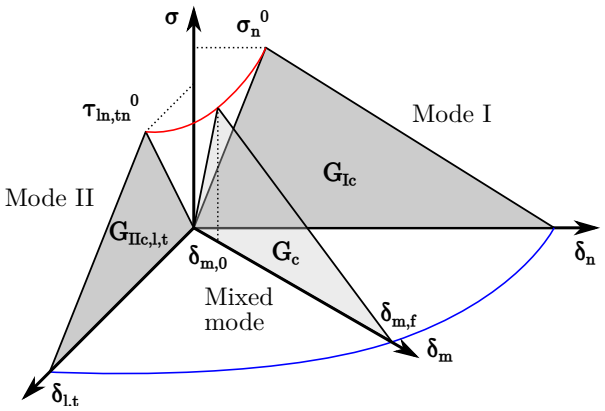

Figure 10: Response in mode I (normal), mode II (shear) and mixed mode for cohesive elements

The out-of-plane elastic moduli were taken equal to the transverse modulus of the ply: $E_n^{coh} = G_{ln}^{coh} = G_{tn}^{coh}$=9.4 GPa. With the fictive thickness t=0.018 mm, a correct flexure modulus was retrieved in comparison with three-point bending tests.

The stress state of the interface is computed from the displacement jumps Δu_l, Δu_t (shear) and Δu_n (normal) by the relationship

$$\begin{bmatrix} \tau_{ln} \\ \tau_{tn} \\ \sigma_n \end{bmatrix} = \begin{bmatrix} K_{II} & 0 & 0 \\ 0 & K_{II} & 0 \\ 0 & 0 & K_I \end{bmatrix} \begin{bmatrix} \Delta u_l \\ \Delta u_t \\ \Delta u_n \end{bmatrix} \tag{1}$$

where $K_{II} = K_I = E_n^{coh}/t$ stand for the stiffness of the interface.

Damage is initiated in a cohesive element when the quadratic stress criterion

$$\left(\frac{\langle \sigma_n \rangle_{>0}}{\sigma_n^0}\right)^2 + \left(\frac{\tau_{ln}}{\tau_{ln}^0}\right)^2 + \left(\frac{\tau_{tn}}{\tau_{tn}^0}\right)^2 = 1 \tag{2}$$

is reached (σ_n^0 is the initiation stress in pure mode I, τ_{ln}^0 the initiation shear stress in pure mode II, direction $\boldsymbol{l}$ and τ_{tn}^0 the initiation shear stress in pure mode II, direction $\boldsymbol{t}$).

The propagation is performed through a linear damage evolution law, with the expression proposed by Camanho and Dávila [22]

$$d = \frac{\delta_m^f \left(\delta_m^{max} - \delta_m^0\right)}{\delta_m^{max} \left(\delta_m^f - \delta_m^0\right)} \tag{3}$$

where δ_m^{max} is the equivalent mixed displacement jump attained through history, δ_m^0 is the equivalent displacement jump at initiation and δ_m^f is the equivalent displacement jump at failure.

At last, the Benzeggagh and Kenane [24] criterion is used in order to predict delamination and account for mode-mixity

$$G_{Ic} + (G_{IIc,l} - G_{Ic}) \left(\frac{G_{II,l} + G_{II,t}}{G_I + G_{II,l} + G_{II,t}}\right)^{\eta} = G_c \tag{4}$$

with G_{Ic} being the critical fracture energy in pure mode I, $G_{IIc,l} = G_{IIc,t}$ the critical fracture energies in pure mode II, G_I, $G_{II,l}$ and $G_{II,t}$ the fracture energy states in mode I, mode II direction $\boldsymbol{l}$ and mode II direction $\boldsymbol{t}$ and, at last η, a material parameter.

The values of the critical fracture energies G_{Ic} and $G_{IIc,l} = G_{IIc,t}$ were identified with DCB and ENF tests following ASTM D5528 [25] and ASTM D7905 [26] recommendations. The tests were carried out for each interface of interest: 0/45, 45/90 and 90/90 by following the recommendations of Sebaey et al. [27] in order to prevent crack jumping. The stacking sequence of the DCB and ENF specimens were respectively [45/-45/0_{10}/-45//$0/90_2/0_8/90_2$/0], [45/-45/0_8/-45/45//90/90/0_8/90_2] and [$90_2/0_8$/90/90//90/90/0_8/90_2]. An inverse identification technique, relying on meshes of characteristic size 1 mm in the plan of the specimen, was used to finalize the determination of the initiation stresses σ_n^0, τ_{ln}^0 and τ_{tn}^0. For the power parameter η, that accounts for mixed modes, a value of 0.5 was taken by inverse identification upon the unfolding of the L-shaped specimens. All the values are gathered in Tab. 3.

Property	Unit	Value		
		0/45	45/90	90/90
G_{Ic}	mJ.mm^{-2}	0.49	0.49	0.49
$G_{IIc,l} = G_{IIc,t}$	mJ.mm^{-2}	1.05	1.25	1.05
η	-	0.5	0.5	0.5
σ_n^0	MPa	25 / 70*	20 / 65*	30 / 75*
$\tau_{ln}^0 = \tau_{tn}^0$	MPa	55 / 135*	50 / 130*	30 / 110*

Table 3: Material properties for the mechanical behaviour of the interfaces (*: for initiation normal and shear stresses, noted x / y, x stands for the value for 1 mm elements whereas y is for 2 mm elements along the specimen)

4.2. Mesh considerations and loading conditions

Since the curved composite beams studied are of large dimensions, and with the aim to be able to re-use the proposed approach on larger structures in the future, the choice was made to use a relatively coarse mesh of size 1 mm along the specimen (constant 1 mm for the width) in the plane of the ply at the level of the inner arc. Since the shape of the specimen is convex, this lead to elements of size 1.8 mm (still 1 mm width) at the level of the outer arc.

To avoid premature delamination in the larger elements, a pragmatic approach consisting in introducing a dependence of the initiation stresses (σ_n^0, τ_{ln}^0 and τ_{tn}^0) to the mesh size was implemented. Hence, the values presented in Tab. 3 with the form x / y* correspond to x: values for 1 mm mesh and y: values for 2 mm mesh. For the elements of size comprised between 1 and 2 mm, a linear interpolation was used. To limit the number of sections to be created, 5 families of material parameters were defined as a function of the mesh size: (1) between 0.9 and 1.1 mm, (2) between 1.1 and 1.3 mm, (3) between 1.3 and 1.5 mm, (4) between 1.5 and 1.7 mm, and, at last (5) between 1.7 and 1.9 mm.

For the loading of the specimens, the top and bottom cylinders were modelled as analytical rigid bodies. A normal law for contact, without friction, was used between the cylinders and the arms of the specimens. The bottom cylinders were embedded whereas the displacement of the top cylinders was imposed. Specific boundary conditions were imposed on three particular nodes of the specimen to prevent rigid body motions without introducing artificial stresses in the model. A geometrically non-linear framework was used to solve the problem with Abaqus/Standard. The analysis were performed using 2 CPUs (20 cores) Intel Xeon E5-2680v2 2.8GHz with 64GB RAM on CALMIP EOS super-computer. The parallelization parameters were chosen after a scalability study. Each computation lasted around 10 hours (up to 200 hours of CPU time).

4.3. Numerical results

The specific load versus displacement curves obtained from the model are plotted in the Fig. 11. The experimental associated curves are also present for comparison.

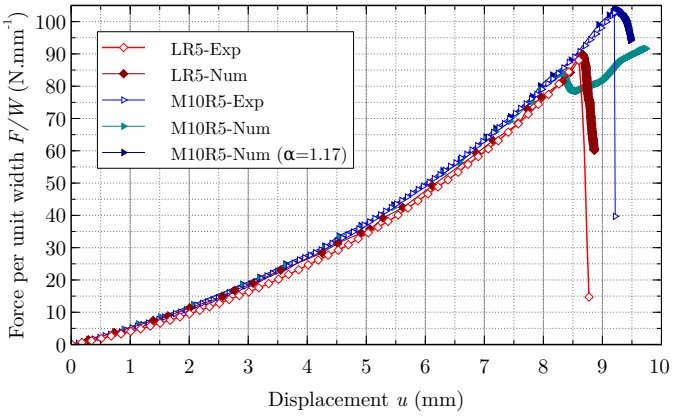

Figure 11: Comparison between experimental and numerical load per unit width F/W versus displacement u curves for LR5 and M10R5 specimens

As a first observation, the model appears to be able to reproduce accurately the elastic non-linear stiffening part of the mechanical response of the specimens. The stiffness is indeed well recovered which validates the elastic properties of the model. Concerning the sharp drop of load at failure, the model is quite predictive for the LR5 specimen. However, with the same material parameters (curve labeled M10R5-Num) the failure appears prematuerly for M-shaped specimen, with a capability of load recovery that is not representative of what was observed in experiments. If the initiation stress values are scaled by a factor α=1.17 determined empirically by trial-and-error strategy upon FE analyses, a correct level of load at failure is obtained, as can be seen from curve M10R5-Num (α=0.17). Hence, the model is not yet capable of predicting the correct level of load at failure for all the geometries. This issue is not surprising. Nguyen et al. [15] already highlighted the very strong dependence and sensitivity of this quantity to the parameters of the model.

The second observation concerns the failure scenario. The Fig. 12 presents the delaminated areas of the LR5-Num model

at increasing iterations of the calculation. The stacking sequence is recalled on the left and a zoom of the specific load versus displacement curve is on the top of the figure. The A, B, C, D, E and F sub-figures present the state of the specimen at the points designated on the specific load versus displacement curve. Only the interfaces of the specimen are represented by quarter. The visible interfaces are as follows: bottom right quarter: 3 first interfaces, top right quarter: 6 first interfaces, bottom left quarter: 10 first interfaces and top left quarter: all the interfaces. Hence, the 3 first -45/90 interfaces are clearly visible on the right and on the bottom of each sub-figure.

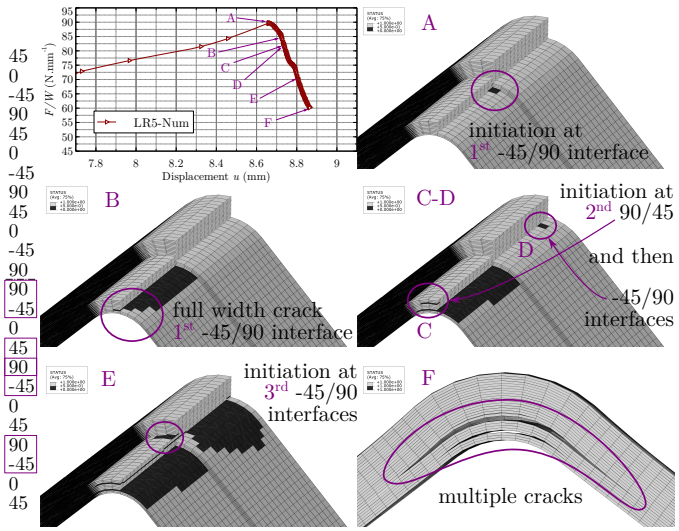

Figure 12: Failure scenario of the L-shaped specimen

The model shows that the delamination starts at the first −45/90 interface, at the centre of the specimen and in the arc (Fig. 12-A). The crack then propagates and reaches the side of the specimen, prior to any other initiation of delamination (Fig. 12-B). In Fig. 12-C-D, two new cracks appear (in few iterations). The second crack initiates at the border of the specimen in the second 90/45 interface (Fig. 12-C) and the third one, near the border of the specimen, in the second -45/90 interface (Fig. 12-D). The three cracks propagate widely before a fourth crack initiation located in the centre of the specimen, on the third -45/90 interface, as illustrated in the Fig. 12-E. In the end, and in adequation with the experimental results, multiple cracks reach the side of the specimen and propagate along the arms as can be seen in the Fig. 12-F which presents the side of the specimen.

As a result, the model seems able to produce the multiple -45/90 or 90/45 delaminated interfaces that were observed experimentally. Beyond that, it allows a better understanding of the failure scenario, the latter being experimentally inaccessible because of its suddenness and brevity. Hence, the delamination failure mode starts in the arc, in the lower -45/90 interface, which is not the weakest one as can be verified in Tab. 3. It corresponds to the peak load. The crack then grows and then other cracks develop in the upper -45/90 or 90/45 interfaces during the load drop.

The failure scenario established by the model for the M-shaped specimen, is now presented in the Fig. 13. The same elements compose the figure and sub-figures.

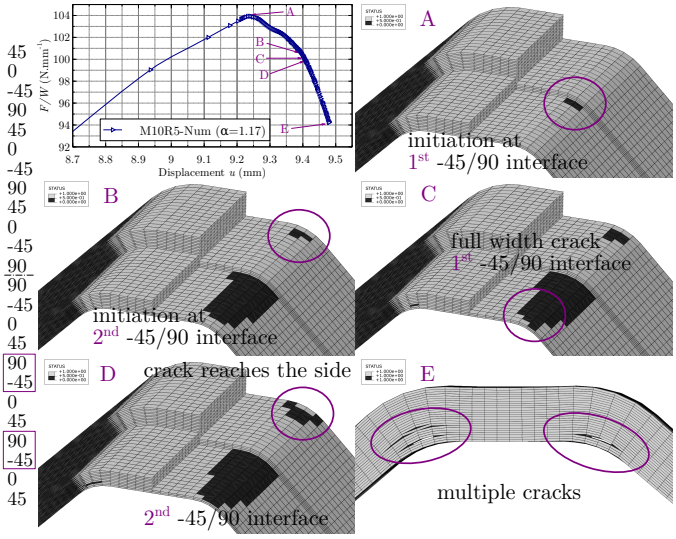

Figure 13: Failure scenario of the M-shaped specimen

The failure scenario is somewhat different from what observed for the L-shaped specimen. The interfaces involved in the failure are -45/90 interfaces (no delamination in the 90/45 interface was observed). Only the first two -45/90 interfaces are delaminated for the M-shaped specimen (instead of three for the L-shaped one). This tendency is similar with the observations made from the tests, where more interfaces were found delaminated for the L-shaped than for the M-shaped specimens.

Another difference concerns the sequentiality of the failure events. In the case of the L-shaped specimen, the first crack crosses the entire width of the specimen prior to any other delamination initiation. This is not the case for the M-shaped specimen. The model shows that the delamination starts at the first -45/90 interface, at the centre of the specimen and in the two radii (Fig. 13-A). These two cracks propagate but, before they reach the side of the specimen, other cracks appear on the second -45/90 interface, near the borders of the specimen (Fig. 13-B). Then, in agreement with the experimental results, the first crack reaches the side of the specimen, at the level of the radii, near the arms (Fig. 13-C) before the second crack does the same (Fig. 13-D). At last, the Fig. 13-F presents the side of the specimen, which highlights multiple cracks as experimentally observed.

From these two numerical studies, and according to the model, it is possible to describe a typical failure scenario for the L- and M-shaped specimens that is not accessible from experiments. Damage (delamination only here) starts in the -45/90 interface (or also in the 90/45 for L-shaped specimen) at the centre of the specimen. It then propagates to cross the entire width of the specimen: prior to any other initiation of delamination for L-shaped, and during other initiations for the M-shaped specimen. In the end, multiple cracks occurred with a higher number of delaminated interfaces for the L-shaped specimen

than for the M-shaped specimen, which presents two areas of damage in each interface layer instead of one.

5. Summary and conclusions

In this work, a pragmatic approach to improve the mechanical strength of curved composite beams have been proposed. It was shown, through experimental tests and numerical models, that the introduction of a flat portion in the arc of singly curved quasi-isotropic composite beams was a simple and effective way to rise the failure load of such structures.

Under the same loading conditions, four-point bending following ASTM D6415/6415M [2] recommendations highlighted a strengthening effect, with a raise of the load at failure of around 15%. A simple two-dimensional, plane strain finite element model was proposed in order to understand what physical phenomenon was involved. It has clearly shown that the key point lied in the introduction of an out-of-plane compression zone located in the flattened area. The splitting of a 90° circle arc into two 45° circle arcs separated by a flat section made it possible to reduce the surface stressed in each 45° arc, and thus to delay the failure. The experimental tests also revealed the failure scenario of the L- and M-shaped specimens: non-linear stiffening elastic behaviour followed by a brutal failure due to unstable and multiple delaminations. Moreover, delamination was shown to start in the area of the junction between the arms and the arc, on the first or the second -45/90 or 90/45 interface, followed by subsequent delaminations also involving -45/90 or 90/45 interfaces.

In the last section, a three-dimensional finite element model based on continuum mechanics and cohesive zones model was developed. The arbitrary choice to use relatively coarse meshes was made in order to be able to handle large structures. The elastic parameters of the model were identified from standard tests such as tensile tests on 0°, 45° and 90° tensile tests. To feed the cohesive zones model, DCB and ENF tests were carried out on the interfaces of interest: 0/45, ±45/90 and 90/90. Associated with a pragmatic approach to deal with the dependency of the cohesive zones model properties upon the mesh size, the proposed approach appeared to be partially able to reproduce the experimental observations. If the model was able to predict accurately the failure load at the first run for the L-shaped specimen, it was not the case for the M-shaped one. A scaling strategy had to be set up for this. However, the model was able to highlight a failure scenario in agreement with experimental observations, made from the side of the specimen. It made it possible to have a more precise idea of the sequence of events leading to failure, with delamination clearly initiated on the first -45/90 interface, then progression on the higher -45/90 (or also 90/45 for L-shaped specimen) interfaces. The proposed modelling strategy therefore provides a useful complement to the tests.

Acknowledgement

The authors acknowledge the supercomputing centre CALMIP for granting access to the HPC resources under the allocation 2017-P12153.

Data availability

The raw/processed data required to reproduce these findings cannot be shared at this time due to legal or ethical reasons. The raw/processed data required to reproduce these findings cannot be shared at this time as the data also forms part of an ongoing study.

References

[1] S. G. Lekhnitskii, Anisotropic plates, Gordon and Breach Science Publishers, 1968.
[2] ASTM, Standard test method for measuring the curved beam strength of fiber reinforced polymer matrix composite, ASTM D6415/D6415M-06a.
[3] K. T. Kedward, R. S. Wilson, S. K. McLean, Flexure of simply curved composite shapes, Composites 20 (6) (1989) 527–536.
[4] R. A. Shenoi, W. Wang, Through-thickness stresses in curved composite laminates and sandwich beams, Composites Science and Technology 61 (11) (2001) 1501–1512.
[5] G. Kress, R. Roos, M. Barbezat, C. Dransfeld, P. Ermanni, Model for interlaminar normal stress in singly curved laminates, Composite Structures 69 (4) (2005) 458–469.
[6] R. Roos, G. Kress, M. Barbezat, P. Ermanni, Enhanced model for interlaminar normal stress in singly curved laminates, Composite Structures 80 (3) (2007) 327–333.
[7] J. M. González-Cantero, E. Graciani, A. Blázquez, F. París, A new analytical model for evaluating interlaminar stresses in the unfolding failure of composite laminates, Composite Structures 147 (2016) 260–273.
[8] W. Cui, T. Liu, J. Len, R. Ruo, Interlaminar tensile strength (ILTS) measurement of woven glass/polyester laminates using four-point curved beam specimen, Composites Part A: Applied Science and Manufacturing 27 (11) (1996) 1097–1105.
[9] W. Hao, D. Ge, Y. Ma, X. Yao, Y. Shi, Experimental investigation on deformation and strength of carbon/epoxy laminated curved beams, Polymer Testing 31 (4) (2012) 520–526.
[10] J. S. Charrier, F. Laurin, N. Carrere, S. Mahdi, Determination of the out-of-plane tensile strength using four-point bending tests on laminated L-angle specimens with different stacking sequences and total thicknesses, Composites Part A: Applied Science and Manufacturing 81 (2016) 243–253.
[11] R. Borg, L. Nilsson, K. Simonsson, Simulation of low velocity impact on fiber laminates using a cohesive zone based delamination model, Composites Science and Technology 64 (2004) 279–288.
[12] J.-H. Kim, K.-H. Nguyen, J.-H. Choi, J.-H. Kweon, Experimental and finite element analysis of curved composite structures with C-section, Composite Structures 140 (Supplement C) (2016) 106–117.
[13] B. Gözlüklü, D. Coker, Modeling of the dynamic delamination of L-shaped unidirectional laminated composites, Composite Structures 94 (4) (2012) 1430–1442.
[14] P. P. Camanho, C. G. Davila, M. F. de Moura, Numerical Simulation of Mixed-Mode Progressive Delamination in Composite Materials, Journal of Composite Materials 37 (16) (2003) 1415–1438.
[15] K.-H. Nguyen, H.-W. Ju, V.-H. Truong, J.-H. Kweon, Delamination analysis of multi-angle composite curved beams using an out-of-autoclave material, Composite Structures 183 (Supplement C) (2018) 320–330.
[16] G. Alfano, M. A. Crisfield, Finite element interface models for the delamination analysis of laminated composites: mechanical and computational issues, International Journal for Numerical Methods in Engineering 50 (7) (2001) 1701–1736.
[17] A. Turon, C. Dvila, P. Camanho, J. Costa, An engineering solution for mesh size effects in the simulation of delamination using cohesive zone models, Engineering Fracture Mechanics 74 (10) (2007) 1665 – 1682.
[18] L. L. Peng, J. X. Gong, K. J. Wong, L. Guillaumat, Application of cohesive-zone models to delamination behaviour of composite material, World Journal of Engineering 9 (2) (2012) 109–118.

[19] B. Gözlüklü, I. Uyar, D. Coker, Intersonic delamination in curved thick composite laminates under quasi-static loading, Mechanics of Materials 80 (Part B) (2015) 163–182.
[20] ASTM, Standard test method for tensile properties of polymer matrix composite materials, ASTM D3039/3039M.
[21] ASTM, Standard test method for in-plane shear response of polymer matrix composite materials by tensile test of a 45° laminate, ASTM D3518/D3518M.
[22] P. P. Camanho, C. G. Dávila, Mixed-mode decohesion finite elements for the simulation of delamination in composite materials, Tech. Rep. TM-2002-211737, NASA (2002).
[23] F. Pascal, O. Dorival, P. Navarro, S. Marguet, J.-F. Ferrero, Impact damage prediction in thin woven composite laminates part i: Modeling strategy and validation, Composite Structures 190 (2018) 32 – 42.
[24] M. Benzeggagh, M. Kenane, Measurement of mixed-mode delamination fracture toughness of unidirectional glass/epoxy composites with mixed-mode bending apparatus, Composites Science and Technology 56 (4) (1996) 439 – 449.
[25] ASTM, Standard test method for mode I interlaminar fracture toughness of unidirectional fiber reinforced polymer matrix composites, ASTM D5528-13.
[26] ASTM, Standard test method for determination of the mode II interlaminar fracture toughness of unidirectional fiber reinforced polymer matrix composites, ASTM D7905/D7905M-14.
[27] T. A. Sebaey, N. Blanco, C. S. Lopes, J. Costa, Numerical investigation to prevent crack jumping in Double Cantilever Beam tests of multidirectional composite laminates, Composites Science and Technology 71 (13) (2011) 1587–1592.